DOE/ER/45184--T1

DE93 003126

THE ROLE OF GRAIN BOUNDARY CHEMISTRY AND STRUCTURE IN THE ENVIRONMENTALLY-ASSISTED INTERGRANULAR CRACKING OF NICKEL-BASE ALLOYS

Progress Report
for the period August 1, 1991 - July 31, 1992

G. S. Was

Department of Nuclear Engineering
The University of Michigan
Ann Arbor, MI 48109

July, 1992

Prepared for

THE U.S. DEPARTMENT OF ENERGY
AGREEMENT NO DE-FG02-85ER45184

DISCLAIMER

This report was prepared as an account of work sponsored by an agency of the United States Government. Neither the United States Government nor any agency thereof, nor any of their employees, makes any warranty, express or implied, or assumes any legal liability or responsibility for the accuracy, completeness, or usefulness of any information, apparatus, product, or process disclosed, or represents that its use would not infringe privately owned rights. Reference herein to any specific commercial product, process, or service by trade name, trademark, manufacturer, or otherwise does not necessarily constitute or imply its endorsement, recommendation, or favoring by the United States Government or any agency thereof. The views and opinions of authors expressed herein do not necessarily state or reflect those of the United States Government or any agency thereof.

MASTER

DISTRIBUTION OF THIS DOCUMENT IS UNLIMITED

TABLE OF CONTENTS

Page

1. STRESS CORROSION CRACKING EXPERIMENTS on Ni-xCr-9Fe-yC 3

RESULTS
1.1 CERT Experiments in Argon and Water 4
1.2 CLT Experiments in Argon and Water 5
1.3 Oxide Film Formation 5

DISCUSSION
1.4 Creep 6
1.5 Oxide Film 7
1.6 Electrochemical Potential 8

2. DEFORMATION OF C-DOPED Ni-16Cr-9Fe 8

2.1 Constant Load Experiments in Argon 9
2.2 TEM Analysis of CERT Experiments in Argon 10

3. GRAIN BOUNDARY MISORIENTATION STUDIES 10

4. ELECTRON BACKSCATTERING BACKSCATTERING DEVELOPMENT 11

4.1 Image Formation 11
4.2 Image Processing 12

5. REFERENCES 13

6. PUBLICATIONS 14

1.0 STRESS CORROSION CRACKING EXPERIMENTS on Ni-xCr-9Fe-yC

Stress corrosion cracking tests in the form of both constant extension rate tensile (CERT) and constant load tensile (CLT) tests were conducted in either argon, high purity water or water containing 0.001M lithium hydroxide and 0.01M boric acid. The experiments were conducted on a low chromium, nominal chromium and high chromium alloy to determine the susceptibility of these alloys to IGSCC. Experiments in argon were conducted to serve as a baseline in an inert environment and to assess the role of creep at 360°C. Experiments in 0.001M lithium hydroxide and 0.01M boric acid were conducted under controlled potential to determine the role of the electrochemical potential and the reduction of hydrogen at the surface on the cracking susceptibility. These experiments also provide information on the development of the film which will lead to a better understanding of the role of the film in the SCC process.

High purity heats of nickel-base alloys were prepared by the Materials Preparation Center, Ames Laboratory, Iowa State University with compositions given in Table 1. The base alloy is an ultra-high purity heat of Ni-17Cr-9Fe-0.0030C, designated as UHP. A low Cr-containing alloy, designated as LCr (5 wt% Cr) and a high Cr-containing alloy, HCr (30 wt % Cr) were also made. Doping the UHP and HCr alloys with carbon produced the carbon-doped (CD, 312 wppm C) and the high Cr, C-doped (HCrCD, 287 wppm C) alloys. Other impurities were found to exist at very low levels (in wppm: O = 27; Co, Cu, Ti, W = 3; H, N, S < 1). The cast ingot was swaged to a 3.05-mm rod from which tensile bars were prepared. Heat treatments in a flowing argon atmosphere were designed to place all of the carbon into solution.

Cold work was introduced into most of the samples used in this study. The gage section (2.2 mm diameter, and 14.3 mm gage length) of the cylindrical tensile specimens was compressed in the thickness direction by a two-step compression operation to produce a 30% reduction in thickness. The first compression step produced flats in the gage section. The samples were annealed and heat treated in order to obtain the desired microstructure and then a 30% reduction in thickness was achieved in the second compression step. This type of deformation is known to enhance IGSCC susceptibility in water at elevated temperatures, [1,2] and allows direct comparison with previous SCC studies [1].

CERT experiments with an initial strain rate of $3 \times 10^{-7}\ s^{-1}$, were conducted in argon and in high purity (18 mΩ), hydrogenated (0.1 MPa or 16 cc/kg water), deaerated (<10 ppb O_2) water at 360°C. Controlled potential CERT experiments were performed in deaerated, hydrogenated 0.001M lithium hydroxide and 0.01M boric acid water at 360°C. The potential was controlled using an EG&G Model 273 Potentiostat with a Model 276 Interface. The reference electrode was a 0.51 mm platinum wire located within the 52 gage platinum mesh counter electrode that encircled the gage length of the specimen at a distance of 8 mm. The reference electrode was positioned approximately 1 mm from the gage length of the specimen in order to minimize the IR drop from the 100 Ω-cm environment.

One of the high purity water CERT facilities was modified to perform constant load experiments. A special load pan was designed to be screwed onto the bottom pull rod of the autoclave. A load platform was designed to support the load pan when applying the load. When all weights are in place, the platform is lowered smoothly and without excessive shock. Friction between the pull rod and the seal was reduced by installing a single-point contact seal obtained from Bal-Seals Engineering. This type of seal not only provides low friction between the pull rod and the seal but also ensures against leakage. To achieve better pressure control in the system, which affects the load acting on the specimen, a back pressure regulator (BPR) replaced a pressure relief valve in the system. With the BPR, the pressure control in this system is within 10 psi at a temperature of 360°C and a pressure of 2850 psi. Applied load is monitored using a 200 lb full

scale (F.S.) load cell. A special cooling seat unit was designed to house the load cell on top of the autoclave cooling jacket in order to shorten the length of the pull rod which was found to affect the creep strain measurement as the room temperature in this laboratory changes. A problem of thermal effect on the creep strain measurement was eliminated by thermal compensation technique. The technique employs two sets of a Super Linear Variable Capacitance (SLVC) type transducer and a signal conditioner which behave identically when subjected to the same thermal conditions. The two transducers, a reference and a displacement transducer, were mounted side by side parallel to the bottom pull rod during the experiment. The reference transducer was fixed to monitor the effect of temperature variations on the transducer during the course of the experiments. Its output signal was then used to compensate from the output of the displacement transducer which inevitably affected by the same temperature variations in the laboratory.

Tests were monitored with a MacIntosh Plus via a data acquisition bridge supplied by Anson Industries. Software was written to collect data periodically. Specimen dimensions and sampling rates were set by the experimenter at the beginning of each test. Specimen displacement, system pressure, water temperature, room temperature, load, and time were printed out and written to the hard drive simultaneously. Constant load tests were performed in argon and high purity, hydrogenated, deaerated water at 360°C.

After a mechanical test, the sample was ultrasonically cleaned in high purity water before being examined by scanning electron microscopy (SEM) and x-ray photoelectron spectroscopy (XPS). The percentage of the fracture surface showing intergranular failure was determined by SEM photographs at 130 to 150X. Chemical composition, structure and thickness of the surface films were determined using x-ray photoelectron spectroscopy (XPS). The XPS results were obtained using a Mg K_α x-ray source. Depth profiling was done using 3 keV argon ions from a rastering gun at a sputter rate calculated to be 5.0 nm/min using an ion flux of 10 $\mu A\ cm^{-2}$.

RESULTS

1.1 CERT Experiments in Argon and Water

A summary of the CERT experiments is presented in Table 2 for the argon environment and Table 3 for the water environment. In order to compare the % elongation to failure in argon and water, the amount of unmeasured elongation due to 225 MPa of stress applied to the sample from the pressurization of the water had to be considered. This was simply done by assuming the materials exhibit similar elongation up to 225 MPa in both environments and truncating the argon data at 225 MPa. From Tables 2 and 3, the maximum stress and % elongation values tend to be slightly higher in argon than water. This may be attributed to the ability of the water to enhance the IG cracking of the LCr and UHP alloys and the statistical variation of these measurements. As the chromium content is increased from 5 to 16 to 30 wt %, the % IG failure on the fracture surface decreases in both environments. The % IG fracture also decreases for the Ni-16Cr-9Fe and Ni-30Cr-9Fe alloys when the carbon in solution is increased to 300 wppm. These results clearly show that increased levels of Cr and C improve the IG cracking behavior of these alloys at 360°C. In comparing the results of Tables 2 and 3, the role of the environment is realized. The alloys strained in argon exhibit the same or less % IG fracture as those strained in water.

Table 4 shows the role of the environment in IG cracking. At open circuit potential, the % IG cracking is greater in the high purity water than in the $LiOH+H_3BO_3$ water environment. In terms of the applied potential, the UHP alloy shows a slight increase in the % IG cracking as the potential decreases. In the LCr, UHP and HCr alloys, the most IG cracking in a water environment was observed at the lowest potential.

1.2 CLT Experiments in Argon and Water

Figure 1 shows a strong correlation between the steady state creep rate and the alloy chromium content in argon at 360°C. At any given stress, the steady state creep rate varies by several orders of magnitude due to chromium alone. The power-law equation [3] describes the stress dependence of these data through the stress exponent, n, which is greater than 1 for all of the alloys studied.

Figure 2 shows the constant load creep curves of Ni-16Cr-9Fe-10wppmC (UHP6 - 110 micron grain size) conducted in 360°C high purity, deaerated, hydrogenated water at 495 and 462 MPa, and in argon environment at 495 MPa. The constant load creep curves exhibit distinctive primary, secondary, and tertiary creep stage. The most striking result is that the time to creep rupture of the sample conducted in argon was approximately 3 times longer at 495 MPa (see Fig. 1); however, the steady-state creep rate in the two environments is not statistically different. The fracture surfaces of two crept samples in HPW were investigated and found to contain slightly different amount of IG cracking, 32% in the water and 26% in the argon environment. Schuster et al. [4] showed that hydrogen reduced the creep rupture lifetime of the 100%Ni and Ni-25%Fe by as much as 80%. However, the role of hydrogen was not clearly identified. A relationship between log of primary creep and log of time was found to follow Andrade law [5] which can be written as:

$$\varepsilon = c\,t^{n} \qquad (1)$$

where ε is creep strain, c and n is time hardening constant and t is time. The n value was found to be a function of applied stress and environment. A typical plot of the log of primary creep versus the log of time is shown in Fig. 3. Table 5 summarizes results of constant load creep experiments in 360°C water and argon environment. It is evident that the water environment enhances the creep process. The effects of the high purity, deaerated, hydrogenated water are to accelerate the primary creep regime, slightly increase the minimum creep rate, and reduce the creep rupture lifetime.

Figures 4a, b, and c show the fracture surface, side surface and cross section of the UHP alloy after CERT testing in argon at 360°C. Figures 5a, b, and c show the same regions for the UHP alloy after constant load testing at 495 MPa in argon at 360°C. Figures 4a and 5a show the similarity in the fracture surfaces; a faceted appearance with tiny dimples. In the bottom right of Figure 3a is typical ductile rupture. Figures 4b and 5b show that both of the side surfaces exhibit cracking along the grain boundaries. Lines extending from either side of the crack indicate the presence of a grain boundary. In addition, the observation that the slip lines are aligned in different directions on either side of the crack indicate the presence of different grains, and the conclusion that the crack most likely lies on a grain boundary. The fine dimpled structure on the inside surfaces of the crack are similar to those observed on the fracture surface. Figures 4c and 5c show that both cross sections exhibit void formation along the grain boundaries. All of these results indicate that the intergranular failure mode which operates in the CERT test at 360°C is very similar to that which operates in the constant load test at 360°C with a load producing 495 MPa of stress.

1.3 Oxide Film Formation

Figures 6-8 show the composition in atom % vs the sputter time in ESCA in minutes for the gage section of the tensile specimens exposed to deaerated, hydrogenated, high purity and $LiOH+H_3BO_3$ water. The LCr alloy, Figure 6, consistently forms a Ni-rich film while the UHP and HCr alloys form Cr-rich films. Chromium is enriched above the bulk level in the surface film for all three alloys, but especially for the UHP and HCr alloys. For the UHP alloy, the amount of

Cr in the film tends to decrease as the potential was lowered. The Cr-rich film formed on the HCr alloy was similar for both environments and under all potentials. Titanium was found in the surface film of the samples held at -650 mV_{SHE} in LiOH + H3BO3, and is believed to be from the Ti autoclave.

DISCUSSION

1.4 Creep

The presence of grain boundary voids in the cross sectioned specimens, Figure 5c, indicate that a creep mechanism is acting in conjunction with the deformation produced by the slow straining of these alloys. Creep is presumed to be the most likely candidate to form these grain boundary voids due to the inertness of the argon environment, the low level of impurities in the alloy, and the results of the constant load tests which show these alloys to creep in the temperature and stress range of interest. The dominant creep mechanism operating in this study is indicated by a power-law creep relationship,

$$\varepsilon \propto \sigma^n, \qquad (2)$$

where ε is the steady state creep rate, σ is the stress and n is the stress exponent. At temperatures below 0.5 of the melting temperature, dislocation-controlled creep tends to be favored, and the stress exponent is greater than 1. At temperatures above 0.5 of the melting temperature, diffusion-controlled creep tends to favored and the stress exponent is 1. In this study, 360°C is approximately 0.4 of the melting temperature, which is in the dislocation-controlled creep regime. In addition, Figure 1 shows that the stress exponent for all of the alloys studied is greater than 1, an indication that the operating mechanism is power-law or dislocation-controlled creep. These results are in agreement with data obtained on the UHP alloy tested in argon at 400°C [6].

The occurrence of dislocation creep will influence the stress-strain behavior of these materials since both the creep deformation and the deformation due to constant straining occur simultaneously at high stresses. This is best illustrated in the Ni-16Cr-9Fe alloy as a function of the carbon in solution, Figure 9. Due to carbon increasing the amount of solid solution strengthening, it is expected that the higher carbon-containing CD alloy will be stronger and less ductile than the low carbon-containing alloy, UHP. However, this is not the case as the UHP alloy exhibits less elongation to failure. A cross section of the failed specimens indicates that voids formed on the grain boundaries of the UHP alloy, which is believed to be responsible for decreasing the overall ductility. The role carbon plays is shown by constant load tests performed at 430°C at 545 MPa, Figure 10. As the carbon in solution decreases, the creep rate increases and the low-carbon containing alloy will experience more strain damage due to creep than the high carbon-containing alloys. Dislocation creep also influences the mechanical properties as seen by varying the strain rate. Table 6 shows that as the constant extension rate decreases, the % IG failure increases in both argon and water. This illustrates that as the strain rate slows and approaches the steady state creep rate, Figure 8, more strain damage is due to creep, resulting in more IG failure.

The additions of chromium and carbon to nickel-base alloys improve their resistance to IG cracking in both argon and high purity, deaerated, hydrogenated water at 360°C. The improvement in the IG cracking behavior, Table 2, correlates with low steady state creep rates in argon, Figures 1 and 10. This improvement is mainly attributable to the large increase in the creep resistance upon the addition of relatively large amounts of chromium, Figure 1, and small amounts of carbon in solution, Figure 10. It has been argued [6] that for a Ni-16Cr-9Fe alloy, carbon in solution improves the creep resistance by strongly interacting with mobile dislocations, hindering their motion and the creep process. The removal of carbon and the addition of chromium formed

the HCr alloy, which produced the first reported incidence of IG failure of an alloy 690-type material in an inert or high purity water environment. As the carbon content of the HCr alloy is increased, the effect of the carbon is less noticeable because the addition of chromium also improves the IG cracking resistance. Figure 1, shows that the as the Cr content is increased, the steady state creep rate and thus the creep susceptibility is decreased by several orders of magnitude. This result was not totally unexpected since the deformation mechanism maps of Ni as a function of the Cr content show that as the Cr content increases, the power-law creep regime decreases [3]. That is, higher stresses are required to activate power-law creep in the higher Cr containing alloys. So in a CERT test, as the load increases, the onset of creep is delayed so that less time is spent in the creep regime for those alloys with higher amounts of Cr.

The exact mechanism by which Cr improves the creep resistance is unknown, however several possibilities exist. One possible explanation for the improvement in the creep resistance is related to the stacking fault energy (SFE), as illustrated in the Ni-Cr and Ni-Co systems [7,8]. In both systems, an increase in the creep resistance correlates with the addition of Cr or Co, which decrease the SFE. The interpretation of the influence of the SFE on creep is dependent on the physical model chosen for the rate-controlling creep process. However, without reference to any specific creep model, it is likely that the slow creep rates of low SFE metals are due to the relative difficulty of dislocation climb and cross slip [9]. In addition, Cr provides solid solution strengthening which allows the material to achieve higher stresses and presumably a smaller dislocation substructure which is known to improve the creep resistance [10].

Although this study better defines the role of carbon, chromium and creep on the IG cracking behavior of nickel-base alloys, the role of the environment is unknown other than it increases the IG crack susceptibility. Since creep is playing a role in the IG cracking behavior, one possible explanation for the role of the environment involves its effect on the creep process. Companion constant load tests performed in argon and water at 360°C and 495 MPa show a slight change in the steady state creep rate, but a 3-fold decrease in the time to failure in the water environment, Table 5. Although this raises the possibility of the environment enhancing the creep mechanism, the results are preliminary and further experimentation is required. One possibility is that hydrogen is enhancing the onset of the tertiary creep, as concluded in a high temperature creep study of Fe and Ni alloys exposed to helium and hydrogen environments [4].

1.5 Oxide Film

The effect of chromium on surface film formation is shown in Figures 6-8. Increasing the Cr content from 5 to 17 wt. % dramatically changes the surface film from Ni-rich to Cr-rich. An additional increase in chromium from 17 to 30 wt. % does not significantly alter the composition of the surface film. This suggests that there is a critical amount of chromium that controls the dominant surface phase after exposure in deaerated, hydrogenated, high purity and $LiOH+H_3BO_3$ water at 360°C. Gaseous oxidation studies of Ni-Cr alloys have shown that as the Cr content of the alloy increases, the amount of $NiCr_2O_4$ spinel increases, which reduces the flux of nickel through the scale [11]. When the Cr content reaches a critical concentration of about 10 wt.% at 1000°C, the mode of oxidation changes to produce a complete external scale of Cr_2O_3. This phenomena, known as transient oxidation, often affects the selection of only the most stable oxide. Since Cr_2O_3 is more stable than $Ni(OH)_2$ [12,13], it may be that transient oxidation permits Cr_2O_3 to eventually overcome the growth of the $Ni(OH)_2$ as long as a sufficient amount of Cr is present.

1.6 Electrochemical Potential

The effect of the electrochemical potential on the surface film formation and IG cracking behavior is shown in Table 4. For the UHP alloy, the film becomes slightly more Cr-rich and the fracture surface shows slightly more IG cracking as the potential is decreased. In the past, nickel-base alloy 600 has been studied under various pH, potential and stress conditions, without much attention given to the formation of the surface film. In general, there is a trend that as the potential is decreased, the susceptibility to IGC is increased [14-17]. Comparing these conditions with the Ni Pourbaix diagram at 288°C reveals some interesting results, Figure 11. The potential regime where alloy 600 transitions from immunity to IG susceptibility lies very close to the Ni/NiO stability line. The exact location of the Ni/NiO stability line at 360°C is uncertain, but it is reasonably near the 288°C line. It seems possible that the controlling mechanism of IGC is related to the location of the potential with respect to the Ni/NiO stability line. Above the line, NiO is thermodynamically stable, while below the line, Ni metal is stable. The ramifications are that below the Ni/NiO line, no film is stable and the surface should be less protected from environmental attack. Additional information from the alloy 690 system lends support to these results. Alloy 690 contains twice as much chromium as alloy 600 and has been found immune to IGC in many of the same environments that prove detrimental to alloy 600. By comparing the Ni and Cr Pourbaix diagrams at 288°C, Figs. 11 and 12 respectively, there exists a regime where Ni metal is stable and Cr compounds are stable. Therefore, in this region there is a greater likelihood of alloy 690 possessing a stable film than alloy 600.

The results from this study provide information on how the mechanical phenomena of creep influences the IG cracking of nickel-base alloys. However, to be complete, the chemical phenomena of surface film formation should be considered. For instance, results from our lab have shown that the CD alloy with the presumably less protective film, shows very high resistance to IG cracking, while the Cr_2O_3 forming UHP alloy, exhibits low resistance to IG cracking [18]. This may be attributed to the dominating role of creep in the UHP alloy which is suppressed by the addition of carbon. It may be that carbon in solution does more to suppress the creep component and reduce IG cracking by suppressing creep than it does to increase the IG crack susceptibility due to the $Ni(OH)_2$ film. Mechanistically, the mechanical component of creep may dominate the IG cracking behavior of these nickel-base alloys over any chemical component attributable to the surface film formation.

2.0 DEFORMATION OF CARBON-DOPED Ni-16Cr-9Fe

The observation of reduced IG cracking, reduced creep rate and increased strength in carbon-doped Ni-16Cr-9Fe has precipitated a series of experiments which are concentrated on determining the role of carbon in the deformation behavior and failure mode of this alloy. The experiments focus on the UHP alloy and the LCD alloy (110 wppm C), two grain size ranges and the presence or absence of grain boundary carbides. The role of carbon in solution will be addressed by comparing the behavior of the UHP and LCD samples with all carbon in solution. The role of grain boundary carbides will be determined by using a 300 wppm C alloy and heat treating to precipitate all by 110 wppm C at the grain boundary as carbides, thus isolating the role of the carbides.

To begin, samples of the UHP alloy and the LCD alloy (large grain) will be strained in a CERT experiment to the strain which corresponds to the UTS of the UHP alloy. TEM samples will be removed from the gage lengths of these samples to determine the nature of the dislocation cell substructure. A second LCD sample will then be strained to a strain level commensurate with the UTS of the LCD sample. Comparison of the dislocation substructure at these strain levels is expected to lead to some insight as to why the LCD alloy experiences greater strain to failure with

no IG cracking. As a first step in these experiments, CLT experiments are being run in Ar to determine the load conditions needed to induce creep in either the large or small grain sample.

2.1 Constant Load Experiments in Argon

The constant load testing setup consists of a sealed retort containing a transducer which extends to accompany specimen elongation. The transducer produces a voltage change associated with the elongation which can be converted to strain. The closed system is heated to 360°C. Table 8 presents the matrix of five experiments that was created for use with the high purity alloy 600 material in order to isolate the three variables of carbon in solution, intergranular carbides, and grain size. The factor-or-10 difference in grain sizes was achieved by thermomechanical processing. Recrystallization and the absence of intergranular carbides in the fine grained LCD material was verified by TEM analysis. At present, DEPLETE600 code is being used to determine proper heat treatments of a LCD alloy in order to have grain boundary carbides while maintaining 110 ppm carbon in solution. The accuracy of the code will be checked using the TEM to determine the extent of the chromium depletion zone. The results will then be compared to the predicted values.

The experimental setup consisted of an IBM data acquisition system along with a 12 bit board. The resolution of the board is approximately 2.5 millivolts and the equipment has a tendency to produce 2.5 millivolt steps in the creep curve rather than yielding a smooth, continuous curve. The validity of these steps was confirmed with a constant DC voltage source which was increased in one millivolt increments over a period of time and compared with the recorded values. Since there were only a few steps of variable magnitude during tests conducted over many weeks, and the curves were otherwise relatively flat, a more sensitive setup was needed to measure minimum creep rates.

In an effort to distinguish the extremely low creep rates of this carbon doped material from system limitations a Macintosh computer complemented with a board exceeding 12 bit was installed. The resolution of the board is 1 millivolt with steps of only 200 microvolts. During the test run using this new setup, steps did not appear in the plotted data; however, smooth peaks and valleys having amplitudes of several millivolts seemed to occur in cycles of a day or two. Temperature fluctuations were assumed to play a major role in this phenomenon, and correlations have been made between the retort temperature and the recorded voltage. Presently, the effect of thermal fluctuations on voltage is being isolated and will subsequently be subtracted out.

Five constant load tests were initiated for the purpose of attaining creep data for the LCD (110 wppm C) alloy. Three of the five samples were to be initially tested at 550 MPa (approximately 90% UTS), with the option of increasing the stress level in the event that the load was too low to cause creep at 360°C. Unfortunately, all samples broke due to the impact of loading. A scissor jack was then installed as part of the creep setup to provide a smoother loading operation. A fourth sample was tested at 525 MPa for 1500 hours in an effort to resolve a minimal steady state creep rate; however, no time dependent deformation was observed. Yet another specimen was initially loaded to 550 MPa for 150 hours. The stress level was then increased to 565 MPa for an additional 100 hours since the sample did not appear to be creeping. Again, even at this stress value there were no signs of creep. While stepping the stress up to 580 MPa, the sample broke.

Since the large grained carbon doped samples failed by tensile overload instead of creeping, experiments were conducted on a fine grained specimen in order to detect a potential grain size effect. It was expected that the smaller grain size would yield a greater creep rate by grain boundary sliding. The sample experienced 525 MPa for the first 475 hours of the test, after which

the stress was increased to 550 MPa for 150 hours with no evidence of creep. The stress was then raised to 565 MPa and stopped after no creep was observed after 150 hrs. To this point, no creep is observed in the 110 wppm C alloy with either a grain size of 15 or 110 microns. Apparently, the very little C is needed to increase the creep resistance by a sizable amount.

2.2 TEM Analysis of CERT Experiments in Argon

Constant extension rate testing in argon was performed on both ultra high purity material and carbon doped material (300 ppm) using a strain rate of $3x10^{-7}$/sec. Both samples were pulled in tension to 8% at 360° C in an effort to compare the dislocation structures with those of Da Cunha Belo [19]. Foils were cut at a 45° with respect to the stress axis and examined on a JOEL 2000X TEM. Several foils were examined and micrographs were taken of grain boundary areas in both materials at identical crystallographic orientations [(220) off of <001>]. After 8% deformation, there was no clear difference between the dislocation structures of the materials, as is shown in Figures 13 and 14. The formation of a thin oxide layer on the surface of the foil was a source of confusion, for it tended to give planar arrays of dislocations a cellular like appearance. The visibility of the cloud like oxide film changed with sample orientation. Further deformation is required to distinguish between the structures of the two materials and lessen the criticality of the oxide film.

Figure 15 shows the added strength and ductility of the CD alloy as compared to the UHP alloy. The ultimate tensile strength of the UHP alloy occurs at 38% strain, while that of the CD alloy falls at 50% strain. Future plans for TEM analysis include using standard argon CERT conditions for pulling both a UHP and CD sample to 38% prior to foil preparation. By doing so, it will be possible to compare a refined UHP substructure at the onset of necking with a presumably less developed CD substructure at an equivalent amount of total deformation. In addition, another CD sample will be pulled to 50% and examined. This will provide a look at a completely formed CD substructure and can be compared with the other samples.

3.0 GRAIN BOUNDARY MISORIENTATION STUDIES

Constant load experiments were conducted on annealed and CSLB-enhanced samples of UHP Ni-16Cr-9Fe to determine if the CLT test is more aggressive than the companion CERT experiment in terms of IG cracking or the preference for CSL boundaries. Two constant load creep experiments on the annealed sample in 360°C argon atmosphere at 300 MPa were completed. The average minimum creep rate of the two tests is 3.75×10^{-9} sec^{-1} Fig. 2. In order to rule out the boundaries which may crack due to crack propagation, the experiments were stopped by quickly cooling under load at the onset of the tertiary stage. The time to the onset of the tertiary stage is approximately 300 hrs in both tests. SEM revealed that 10 out of 277 characterized boundaries cracked, nine of them were GHABs and one of them was a CSLB (Table 8).

A constant load test of a CSL-enhanced sample was also just completed. The sample was first solution annealed at 1200°C for 1hr. prior to underwent thermomechanical treatments. The treatments consisted of 5% tensile strain + 890°C for 16 hrs. + 3% tensile strain + 890°C for 20 hrs. + 2% tensile strain + 936°C for 11 hrs. The sample was also mechanically polished, electropolished and etched after every heat treatments. This particular thermomechanical steps leaded to 39% of CSLBs. The thermomechanical process resulted in a secondary recrystallization and a grain size of 327 μm; however, the entire sample was not recrystallized which was observed by distorted channeling pattern on some grains. The test was stopped at the onset of tertiary stage after 255 hrs. It was found that a total of 10 out of 216 boundaries were cracked, Table 8. Seven of them are of high angle boundary and the rest are the CSL boundaries. The creep behavior of the

CSL-enhanced sample was very distinct from the solution annealed sample. The most striking difference seems to be in the primary creep regime where recovery and hardening mechanism competes. Almost all of the creep strain was in the primary creep for the CSL-enhanced sample. This regime lasted approximately 75 hrs and accumulate almost 90% of the total strain. As the primary creep exhausted, the creep rate leveled off very rapidly and reached a minimum value of 1.2×10^{-9} sec^{-1}, Fig. 2. Further experiments are in progress to substantiate the difference between the solution annealed and the CSL-enhanced sample in 360°C argon and water environment.

Our previous work has also demonstrated that CSLBs are generally more resistant than GHABs. However, the nature of intergranular cracks has been obscured by the CERTs. In constant load creep experiments, we have found that most of the cracks are of wedge type, and a few of them showed cavities which were lying inside the grain rather than on the boundary, Figs.16 and 17. The geometry of this cracking was recognized by Chang and Grant [20] who showed that the formation of wedge cracks is due directly to grain boundary sliding which has been known to be an important source of creep deformation. Watanabe [21] demonstrated that the amount of sliding strongly depends on the type and misorientation of grain boundaries, and it more easily takes place in GHABs. An explanation for cavities which occurred in the grain is still unclear. However, we commonly observed that slip traces of the grain which contained such cavities always made a shallow angle to the inclined grain boundary. Cavity development may occur as a result of severe incompatibility of grain deformation combined with grain boundary sliding.

If creep were to be responsible for IG cracking found in our sample, dislocation creep would then be favored at our testing temperature and stress level, and the grain boundary sliding model proposed by McLean [22] seems to be appropriate for deformation controlled by dislocation motion. In this model, grain boundary sliding occurs by a mechanism in which lattice dislocations from the grain interior will be held up at the grain boundary and cause sliding by a combination of climb and glide movement in the boundary plane.

4.0 ELECTRON BACKSCATTERING PATTERN DEVELOPMENT

The EBS technique in an Environmental Scanning Electron Microscope (ESEM) is being developed at the University of Michigan in order to extend our IG cracking studies to grain sizes typical of commercial alloys, 20-30 microns. Typically, crystallographic patterns can be observed directly with the low light level camera on a fluorescent screen placed in the scanning electron microscope (SEM) when the sample is approximately 70° tilted and the SEM is in the spot mode [23]. Unlike the SEM, the ESEM operates best in the wet mode, i.e., the chamber is filled with water vapor and the pressure inside the chamber is approximately 5 torr (Typical SEM operates at 1×10^{-6} torr or better). To obtain and optimize the pattern, the process was divided into 2 categories: image formation and image processing.

4.1 Image Formation

The hardware for the image formation consists of the microscope and the fluorescent screen. Because of the configuration of the chamber and the way the ESEM operates, the size of the screen and the screen-to-sample distance has to be restricted. First, the screen-to-sample distance has to be kept small to minimize any scattering events of backscattered electrons with water vapor molecules which may affect the pattern sharpness. However, the distance has to be large enough that the angular distribution of backscattered electrons will provide enough crystallographic information for digitizing purposes. Due to the configuration of the ESEM, the screen must be less than an inch in diameter. From the latest result, the screen of 7/8 in. diameter and the screen to sample distance of 1/2 in. seems to be appropriate.

The quality of the fluorescent screen is very crucial since the image processing step would be meaningless if the image quality were created poorly. The P-20 type phosphor was selected since its wavelength peaks at 550 nm which corresponds to the same peak of visible light that human eyes can perceive. The fiber optics substrate for the phosphor provides a zero depth window, i.e. light generated by the backscattered electrons upon hitting on the phosphor screen will be transmitted axially to the other side of the screen. The quality of the image should therefore be enhanced. Instead of coating aluminum on the screen to prevent charging, a stripe of silver was painted at one edge of the screen to drain electrons out of the screen. We therefore eliminate the potential effect of the thickness of aluminum coating on the pattern.

4.2 Image Processing

Processing the pattern depends largely on the quality of the camera. For our application, we are more interested in determining crystallographic orientation and all we need from the diffraction pattern is to be able to identify the coordinates of two zone axes. Their coordinates along with the pattern center and the screen-to-specimen distance will later be manipulated for obtaining rotation matrices [24]. A CCD-72 series camera built by Dage-MTI Inc. was found to suit our purpose at a reasonable cost. This camera provides a high signal to noise ratio and low light level sensitivity. With its adjustable edge enhancement, contrast, gain and black level offset range, the pattern captured is adequate for our application. Fig.18 shows the EBSP captured on the Macintosh II and was 8 frame averaged with the software (Image 1.44). Software for determining crystallographic orientation is being written for EBSP. A special sample holder design along with its calibration technique is in progress. The current EBS technique developed has a spot size of approximately 1 micron; therefore, this technique will allow us to obtain crystallographic orientation information from commercial alloy which has an average grain size of 30 microns.

5.0 REFERENCES

1. J.K. Sung and G.S. Was, " The Role of Grain Boundary Chemistry in Pure Water Intergranular SCC of Ni-16Cr-9Fe Alloys ", Fourth International Symposium on Environmental Degradation of Materials in Nuclear Power Systems-Water Reactors, National Association of Corrosion Engineers, August 1989, 6-25 to 37.
2. N.E. Paton and W.M. Mahoney, Metall. Trans. 33, 841 (1976).
3. H.J. Frost and M.F. Ashby, Deformation-Mechanism Maps. The Plasticity and Creep of Metals and Ceramics, Pergamon Press, 11 (19??).
4. G.B.A. Schuster, R.A.Yeske, and C.J.Altstetter, Metallurgical Transaction A, 11A (1980) 1657.
5. P.W. Davies and R.Dutton, Acta Metall, 15 (1967) 1365.
6. J.K. Sung, J.W. Jones and G.S. Was, "Effect of Carbon on the Low Temperature Creep Behavior of Ni-16Cr-9Fe", submitted to Metall. Trans as a communication.
7. J. Dennison, R. Llewillyn and B. Wilshire, "The Creep and Fracture Properties of Some Nickel-Chromium Alloys at 600°C", J. Institute of Metals, 95, 115-118 (1965).
8. C.L. Davies, P.W. Davies and B. Wilshire, "The Effect of Variations in Stacking-fault Energy on the Creep of Nickel-Cobalt Alloys", Phil. Mag. 12, 827 (1965).
9. C.R. Barrett and O.D. Sherby, "Influence of Stacking-Fault Energy on High-Temperature Creep of Pure Metals", Trans. of Metall. Soc. of AIME, 233, 1116 (1965)
10. O.D. Sherby, R.H. Klundt and A.K. Miller, "Flow Stress, Subgrain Size, and Subgrain Stability at Elevated Temperature", Metall. Trans., vol. 8A, 843-850 (1977).
11. Introduction to High Temperature Oxidation of Metals, N. Birks and G.H. Meier, Edward Arnold Ltd., London, 107-110 (1983).
12. H. Huschka, G. Luthardt and V. Portscher, "Protective Layers on High-temperature Alloys Against Hydrogen Permeation", Nuclear Technology, 66, 562-569 (1984).
13. K.L. Smith and L.D. Schmidt, "Oxidation and Reduction of Ni-Cr Alloys", J. Vac. Sci. Technol., vol. 20, no. 3, 364-367 (1982).
14. A. Kishida, H. Takamatsu, S. Isobe, K. Arioke and T. Tsuruta, Symposium on Chemistry in High-Temperature Aqueous Solutions, Provo, Utah, August 25-27 (1987).
15. J. Blanchet, J. Coriou, L. Grall, C. Mattieu, C. Otter and G. Turler, Stress Corrosion Cracking and Hydrogen Embrittlement of Iron Base Alloys, 1149-1160.
16. G. Economy, R.J. Jacko and F.W. Pement, "IGSCC Behavior of Alloy 600 Steam Generator Tubing in Water or Steam Tests Above 360 C", Corrosion, vol. 43, no. 12, 727-734 (1987).
17. N. Totsuka and Z. Szklarska-Smialowska, "Effect of Electrode Potential on the Hydrogen-Induced IGSCC of Alloy 600 in an Aqueous Solution at 350 C", Corrosion, vol. 43, no. 12, 734-738 (9187).
18. T.M. Angeliu, J.K. Sung and G.S. Was, Fifth International Symposium on Environmental Degradation of Materials in Nuclear Power Systems-Water Reactors, American Nuclear Society, LaGrange, IL, August 1989, 6-25 to 37.
19. M. Da Cunha Belo, D. Colin, Ph. Berge, Y. Rouillon,"Corrosion sous tension des alliages de haute purete du type Inconel 600",pp.887-893.
20. H.C. Chang and N.J. Grant, AIME Trans., 206 (1956) 544; Journal of Metals, May 1956.
21. T.Watanabe, Metallurgical Transaction A, 14A (1983) 531.
22. D. McLean, Phil. Mag. A, 23 (1971) 467
23. J.A. Venables and C.J. Harland, Phil. Mag. A, 27 (1973) 1193
24. J.A. Venables and R.Bin-Jaya, Phil. Mag. A, 35 (1977) 1317

6.0 PUBLICATIONS IN 1991/92

J. K. Sung and G. S. Was, "Intergranular Cracking of Ni-16Cr-9Fe Alloys in High Temperature High Purity Water," Corrosion, 47 No. 11 (1991) 824-834.

D. C. Crawford and G. S. Was, "Grain Boundary Character Distributions in Ni-Cr-Fe using Electron Channeling Patterns: Methodology and Results", J. Electron Microscopy Technique, 19 (1991) 345-360.

"Grain Boundary Chemistry and Precipitation in Controlled Purity Alloy 690," (with T. Angeliu) in Environmental Degradation of Materials in Nuclear Power Systems - Water Reactors, G. J. Theus and D. Cubicciotti, NACE, Houston, 1991, 5-64 to 5-78.

"The Role of Grain Boundary Chemistry in Pure Water Intergranular Stress Corrosion Cracking of Ni-16Cr-9Fe Alloys," (with J. Sung) in Environmental Degradation of Materials in Nuclear Power Systems - Water Reactors, G. J. Theus and D. Cubicciotti, NACE, Houston, 1991, pp.6-25 to 6-37.

D. C. Crawford and G. S. Was, "The Role of Grain Boundary Misorientation in Intergranular Cracking Behavior of Ni-16Cr-9Fe in Argon and High-Purity Water," Metall. Trans. A, 23A (1992) 1195-1206.

J. K. Sung, J. W. Jones and G. S. Was, "Effect of Carbon on the Low Temperature Creep Behavior of Ni-16Cr-9Fe," Metall. Trans. A, 23A (1992) 1033-1038.

D. C. Crawford and G. S. Was, "The Effect of Grain Boundary Misorientation on Intergranular Cracking of Ni-16Cr-9Fe in 360°C Argon and High Purity Water," Proc. Fifth International Symposium on Environmental Degradation of Material in Nuclear Power Systems -- Water Reactors, American Nuclear Society, La Grange Park, IL, 1992, pp. 488-494.

T. M. Angeliu, J. K. Sung and G. S. Was, "The Role of Carbon and Chromium on the Mechanical and Oxidation Behavior of Nickel-Base Alloys in High Temperature Water," Proc. Fifth International Symposium on Environmental Degradation of Material in Nuclear Power Systems -- Water Reactors, American Nuclear Society, La Grange Park, IL, 1992, pp. 475-481.

J. K. Sung, J. Kochs, and T. Angeliu and G. S. Was, "Effects of Grain Boundary Chemistry on Intergranular Cracking of Ni-16Cr-9Fe in 50% NaOH at 140°C," Metall. Trans. A., in press.

G. S. Was, J. K. Sung and T. Angeliu, "Effects of Grain Boundary Chemistry on Intergranular Cracking of Ni-16Cr-9Fe in High Temperature Water," Metall. Trans. A., in press.

"Microchemical and Microstructural Effects on Stress Corrosion Cracking of Nickel-Base Alloys," Parkin's Symposium, The Minerals, Metals and Materials Society of AIME, Fall, 1991, Cincinnati, OH, in press. **INVITED**

T. Angeliu and G. S. Was, "The Effect of Chromium, Carbon and Yttrium on the Oxidation of Nickel-Base Alloys in High Temperature Water," submitted to J. Electrochem. Soc.

Table 1 Chemical composition of alloys (wt pct)

designation	Ni	Cr	Fe	C	heat treatment
LCr	bal.	5.2	9.1	0.0001	900°C/0.33hr
UHP	bal.	16.7	9.1	0.0029	1100°C/0.33hr
CD	bal.	16.6	9.1	0.0312	1100°C/0.33hr
HCr	bal.	29.7	9.1	0.0019	1050°C/0.33hr
HCrCD	bal.	29.5	9.1	0.0287	1200°C/0.33hr

Table 2 Constant extension rate tensile experiments performed in argon at 360°C at an initial strain rate of $3x10^{-7}$ s^{-1}.

Material Type	max stress MPa	% elong ** after 225 MPa	% IG
LCr*	421	7.0	19
UHP*	520	12.0	14
CD	642	21.9	0
HCr	580	11.6	8
HCrCD	678	14.5	0

* average of 2 tests
** All samples have all been initially compressed by 30%.

Table 3 Constant extension rate tensile experiments performed in high purity, deaerated, hydrogenated water at 360°C at an initial strain rate of $3x10^{-7}$ s^{-1}.

Material Type	max stress MPa	% elong ** after 225 MPa	% IG
LCr	374	6.8	42
UHP*	494	12.8	21
CD	612	25.1	0
HCr*	579	14.5	4
HCrCD	655	14.9	0

* average of 2 tests
** All samples have all been initially compressed by 30%.

Table 4 Constant extension rate tensile experiments performed in argon, deaerated, hydrogenated, high purity water (pH=6) and deaerated, hydrogenated, 0.001 LiOH + 0.01M H_3BO_3 (pH=8) at 360°C at an initial strain rate of $3x10^{-7}$ s^{-1}.

Material Type	Environment	Potential (mV_{SHE})	Max Stress (MPa)	% Elong. <225 MPa	% IG	Film Type
LCr	argon*		421	7.0	19	
	HP water	- 671 OCP)	374	6.8	42	Ni rich
	Li + B	- 650	402	8.4	38	Ni rich
	Li + B*	- 922 (OCP)	404	7.9	49	Ni rich
	Li + B	- 1350	405	8.3	48	Ni rich
UHP	argon*		520	12.0	14	
	HP water*	- 671 (OCP)	494	12.8	21	Cr rich
	Li + B	- 650	520	13.8	24	Cr rich
	Li + B	- 922 (OCP)	523	11.7	29	Cr rich
	Li + B	- 1350	530	12.6	33	Cr rich
HCr	argon		582	16.3	8.0	
	HP water*	- 671 (OCP)	579	14.5	3.6	Cr rich
	Li + B	- 650	598	16.5	2.4	Cr rich
	Li + B	- 922 (OCP)	583	14.0	2.9	Cr rich
	Li + B	- 1350	544	12.6	5.2	Cr rich

* average of 2 tests

Table 5: Summary of constant load creep experiments in 360°C water and argon environment.

Stress (MPa)	Test environment	Min Creep Rate (sec^{-1})	Creep strain (%)	Rupture time (hrs)	Time Hardening Exponent (n)	% IG Cracking
462	HPW	1.08E-9	0.4	397	.25	32
495	HPW	8.98E-9	1.06	127	.5	32
495	Ar	2.7e-9	0.6	340	.33	26

Table 6 Comparing the % IG failure as a function of the strain rate/steady state creep rate for the UHP alloy in argon and water at 360°C.

strain rate (s-1)	argon % IG	water % IG
3×10^{-7}	14	21
1×10^{-7}	25	31
approx. 3×10^{-9}	32	45

Table 7 Experimental matrix on alloy and grain size.

Alloy	100 µm grain size	15 µm grain size	Carbon in Solution (wppm)
UHP alloy 600	X	X	<20
LCD alloy 600	X	X	110
LCD alloy 600 grain boundary carbides		X	110

Table 8 Results of the constant load creep experiments in 360°C argon environment on grain boundary misorientation studies.

Sample	Boundary Type	Min Creep Rate (sec^{-1})	Total Test Time (hrs)	Creep Strain (%)	# Cracked Boundaries
Solution Annealed	GHAB 79% CSLB 18% LAB 3%	3.6E-9	325	0.5	GHAB 9 CSLB 1 LAB 0
CSL enhanced	GHAB 57% CSLB 38% LAB 5%	1.2E-9	255	0.8	GHAB 7 CSLB 3 LAB 0

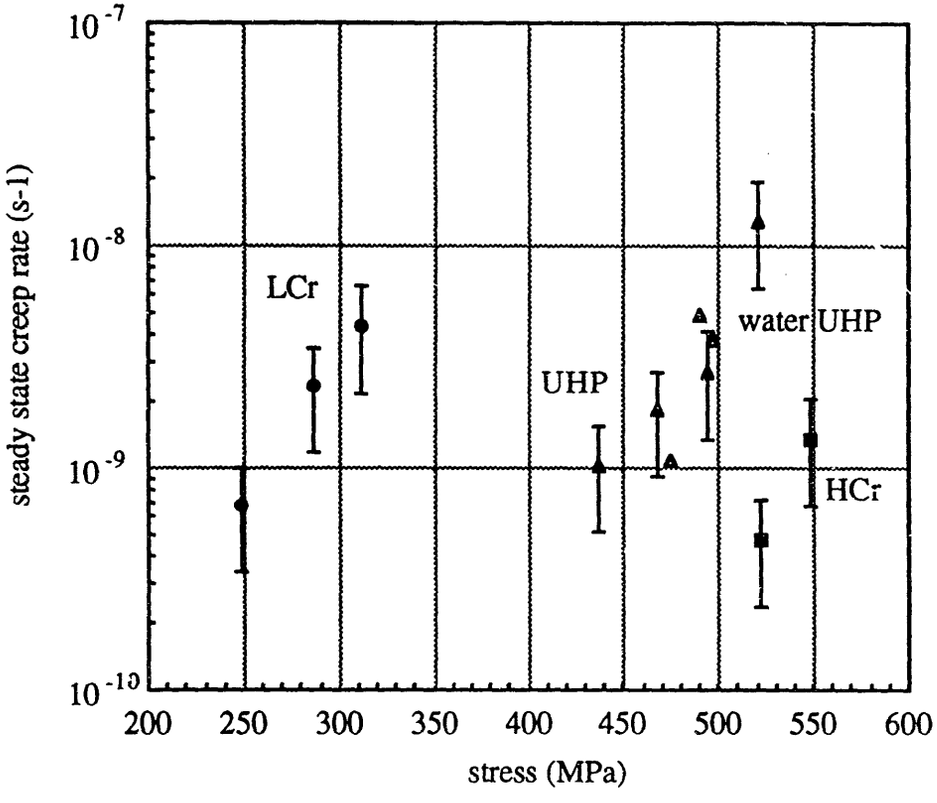

Figure 1 Constant load data in argon and water at 360°C (assumes ± 50 % creep rates in argon)

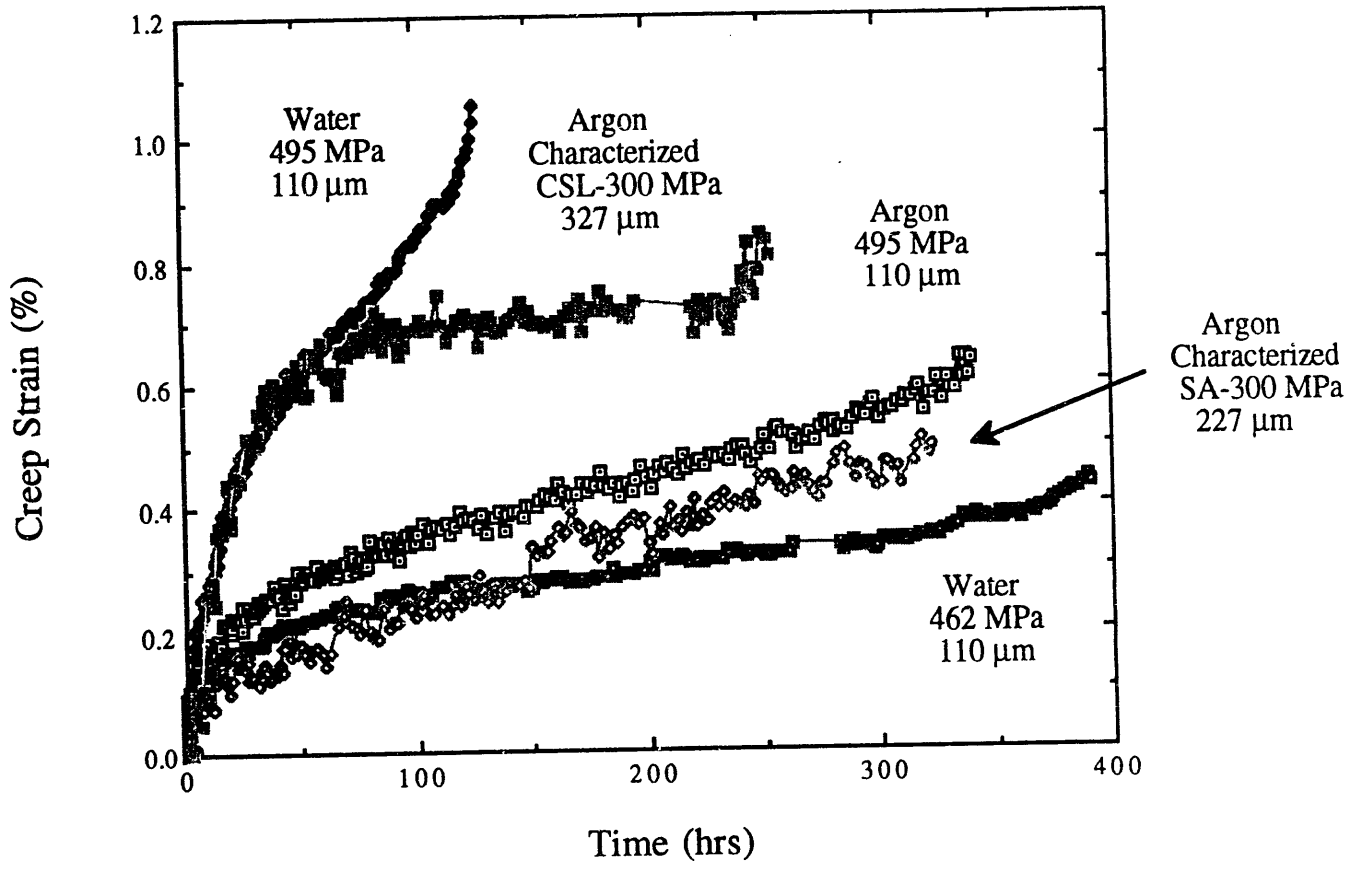

Fig.2 Constant load creep curves of alloy UHP6
in 360°C water and argon environment

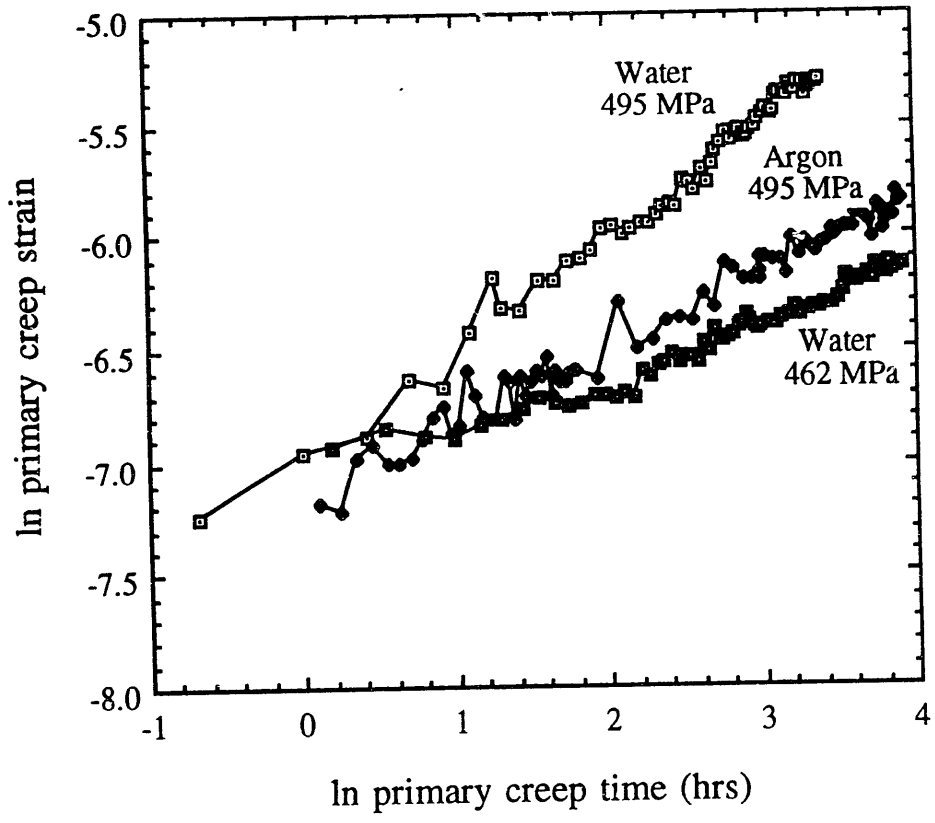

Figure 3 Plot of primary creep relation for alloy UHP6 in 360°C water and argon environment.

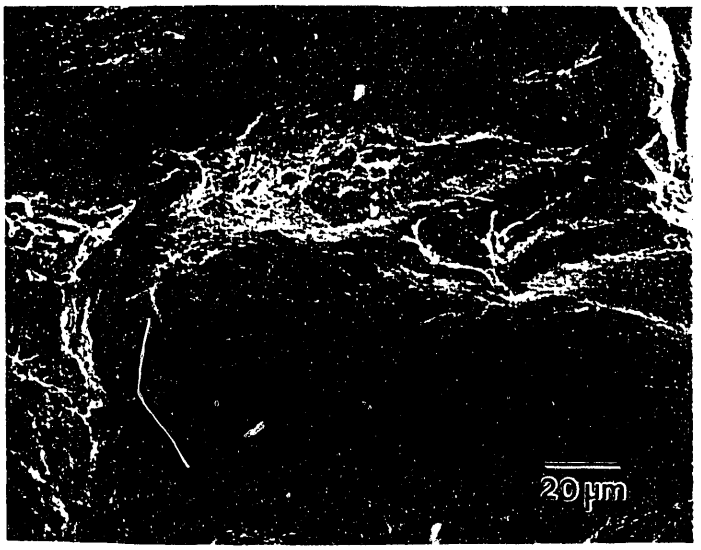

Figure 4a Fracture surface of the UHP alloy, CERT tested in argon at 360°C.

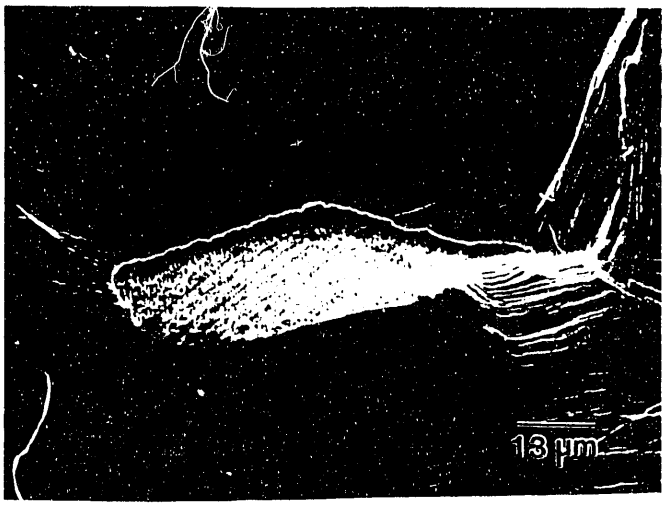

Figure 4b Side surface crack on the UHP alloy, CERT tested in argon at 360°C.

Figure 4c Cross section of the UHP alloy, CERT tested in argon at 360°C.

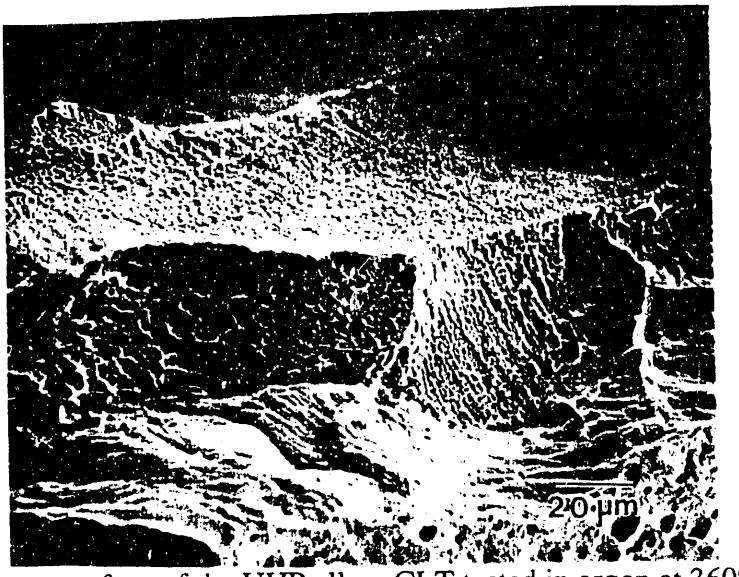

Figure 5a Fracture surface of the UHP alloy, CLT tested in argon at 360°C.

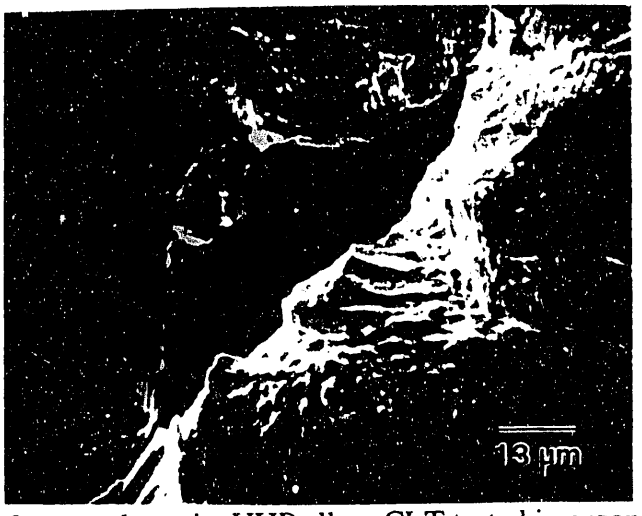

Figure 5b Side surface crack on the UHP alloy, CLT tested in argon at 360°C.

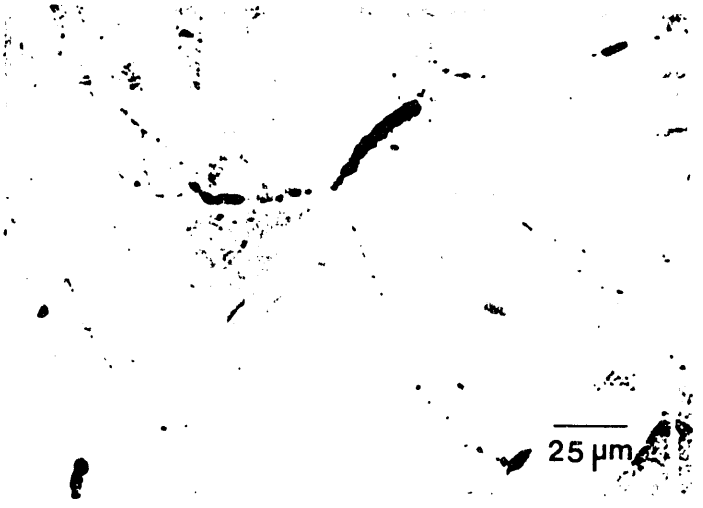

Figure 5c Cross section of the UHP alloy, CLT tested in argon at 360°C.

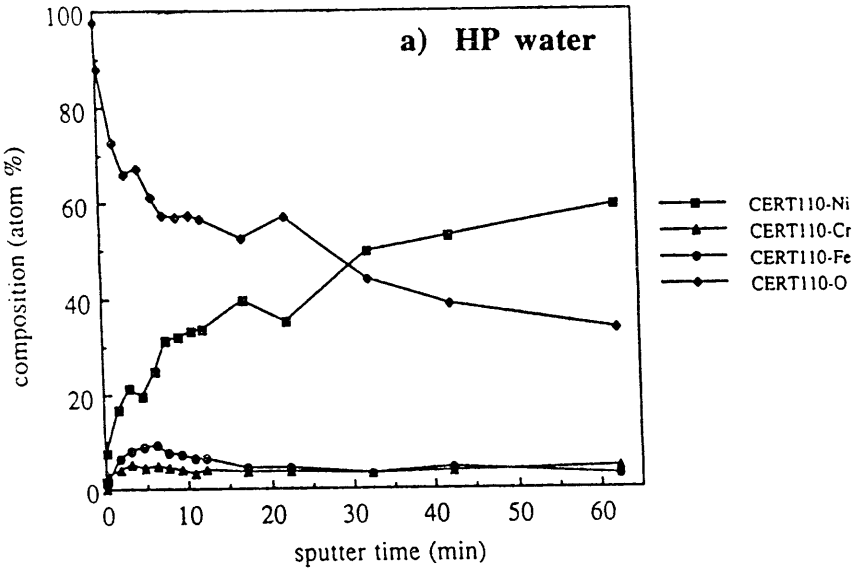

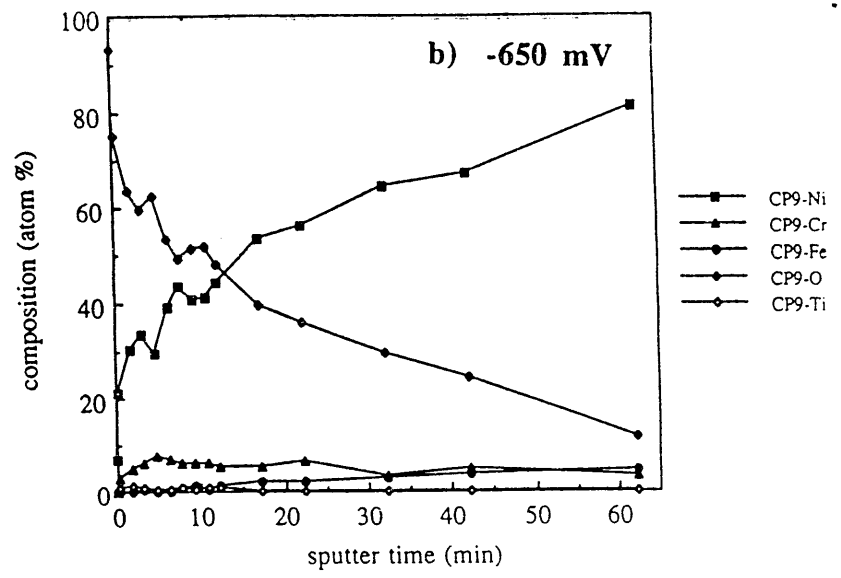

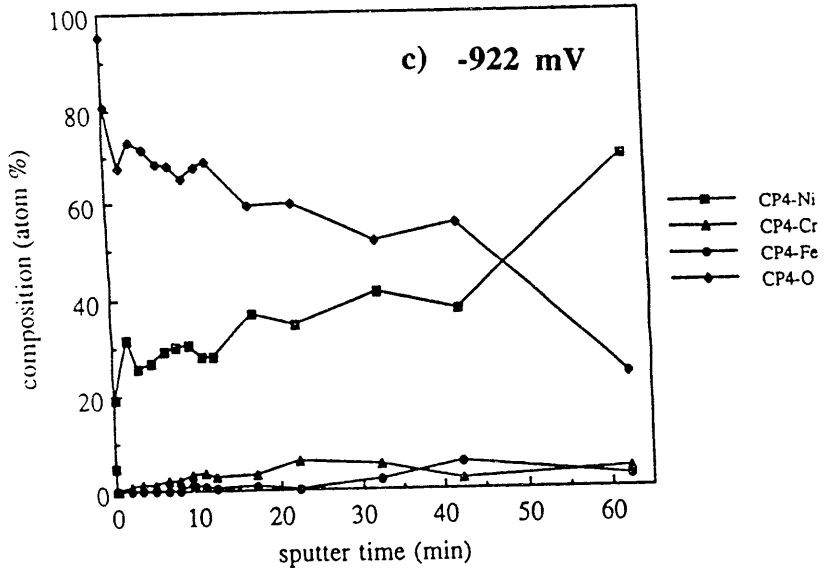

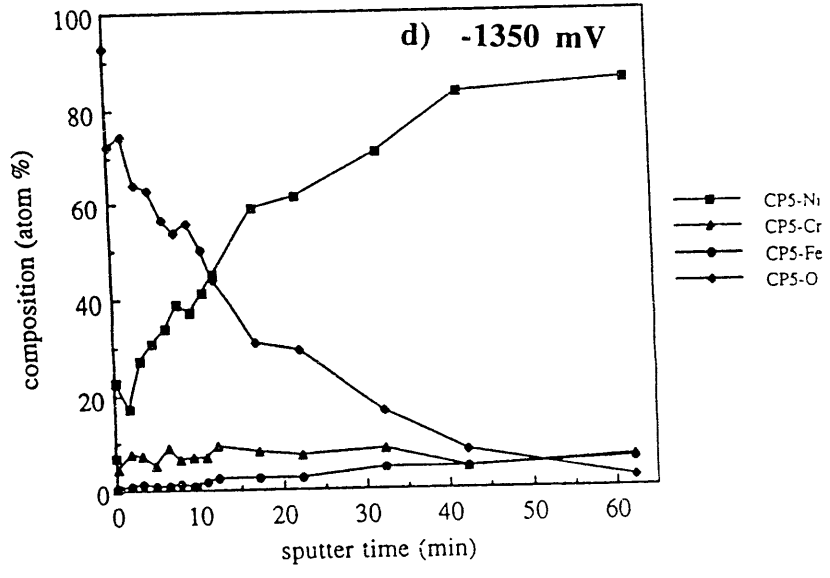

Figure 6 Surface film results from the CERT experiment gage section of the LCr alloy exposed to a) deaerated, hydrogenated, high purity water and deaerated, hydrogenated, LiOH + H3BO3 water at potentials of b) -650mV c) -922 mV and d) -1350 mV with respect to the SHE.

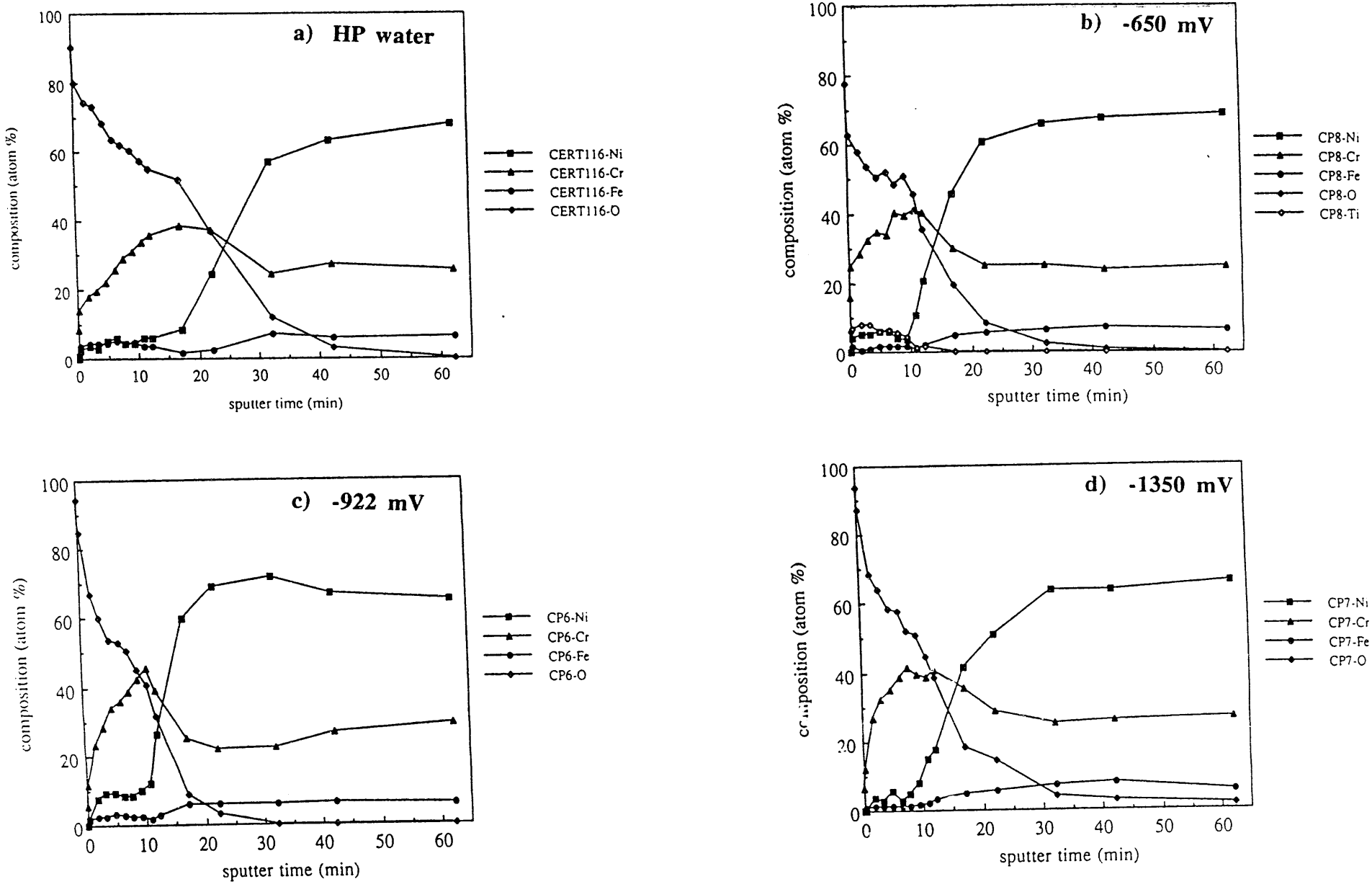

Figure 7 Surface film results from the CERT experiment gage section of the UHP alloy exposed to a) deaerated, hydrogenated, high purity water and deaerated, hydrogenated, LiOH + H3BO3 water at potentials of b) -650mV c) -922 mV and d) -1350 mV with respect to the SHE.

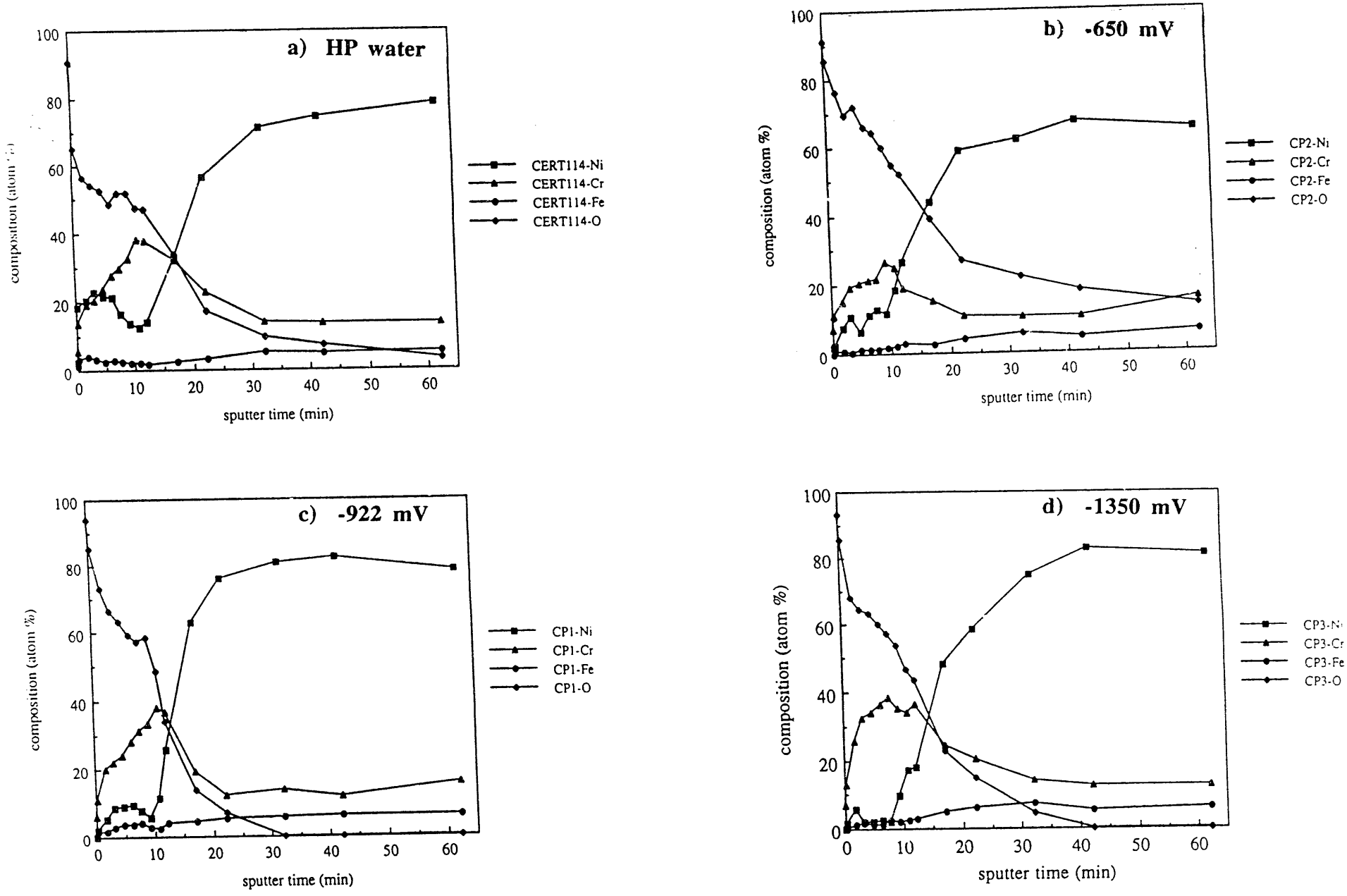

Figure 8 Surface film results from the CERT experiment gage section of the HCr alloy exposed to a) deaerated, hydrogenated, high purity water and deaerated, hydrogenated, LiOH + H3BO3 water at potentials of b) -650mV c) -922 mV and d) -1350 mV with respect to the SHE.

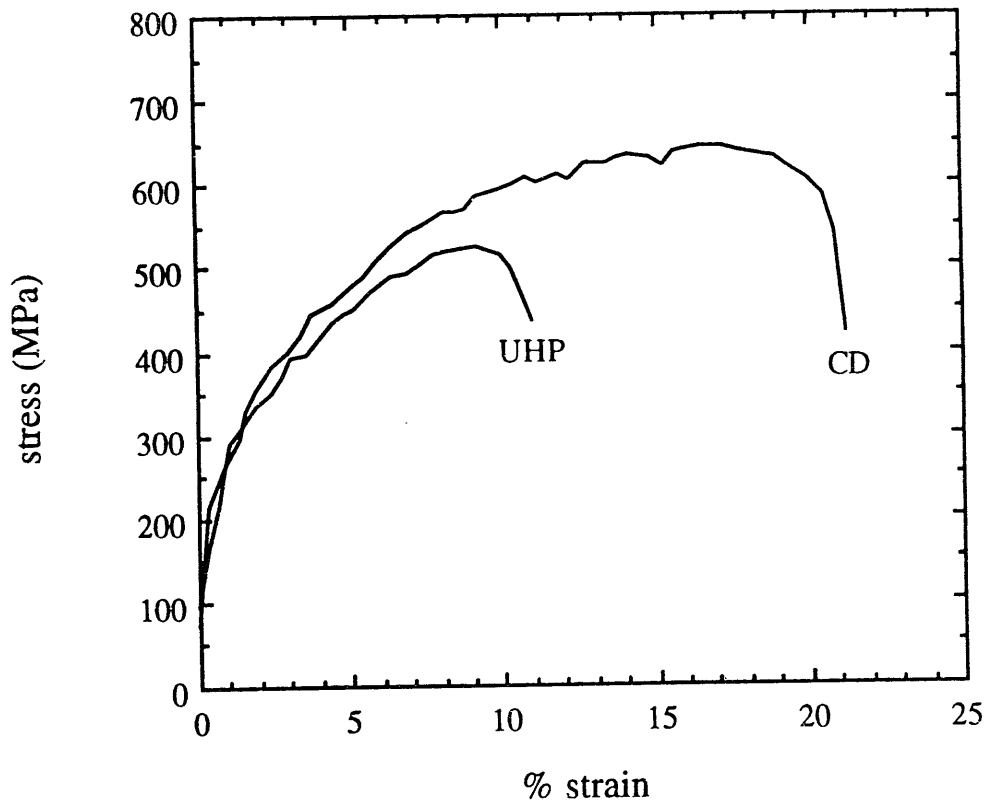

Figure 9 Constant extension rate tensile experiment of the UHP and CD alloys in argon at 360°C at $3 \times 10^{-7}\ s^{-1}$.

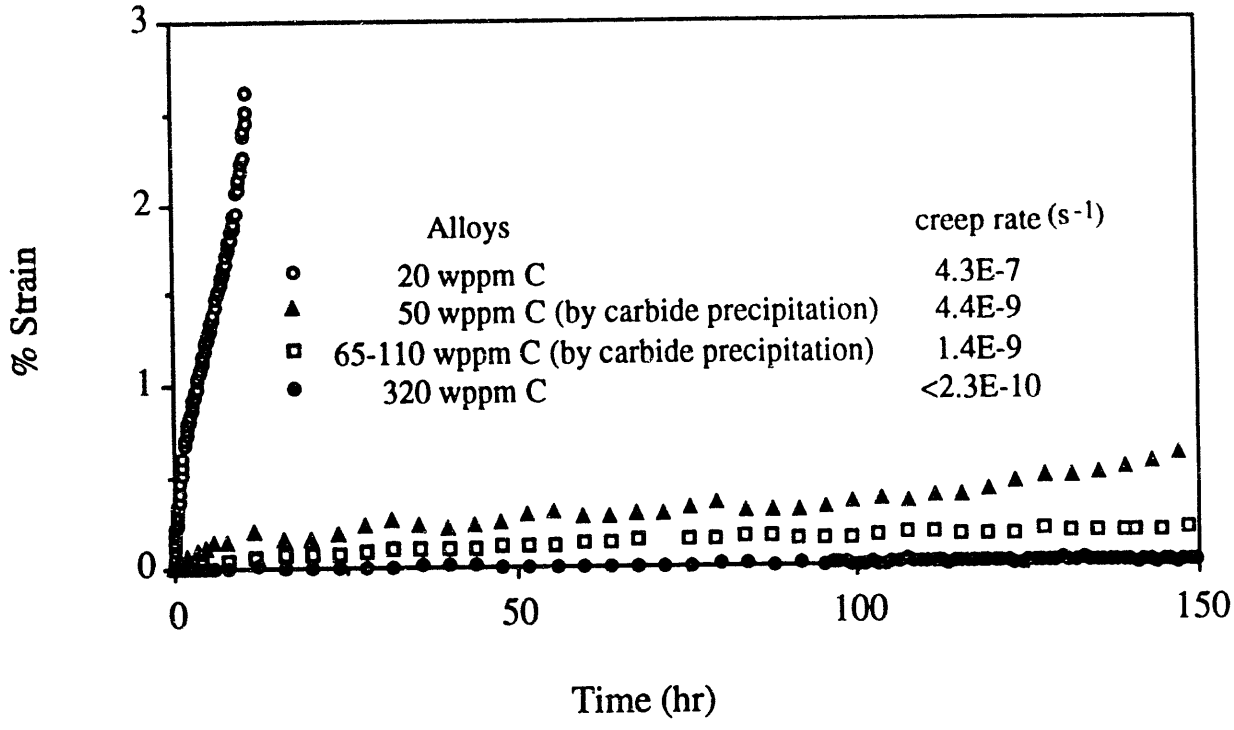

Figure 10 Constant load data in argon at 545 MPa at 430°C.

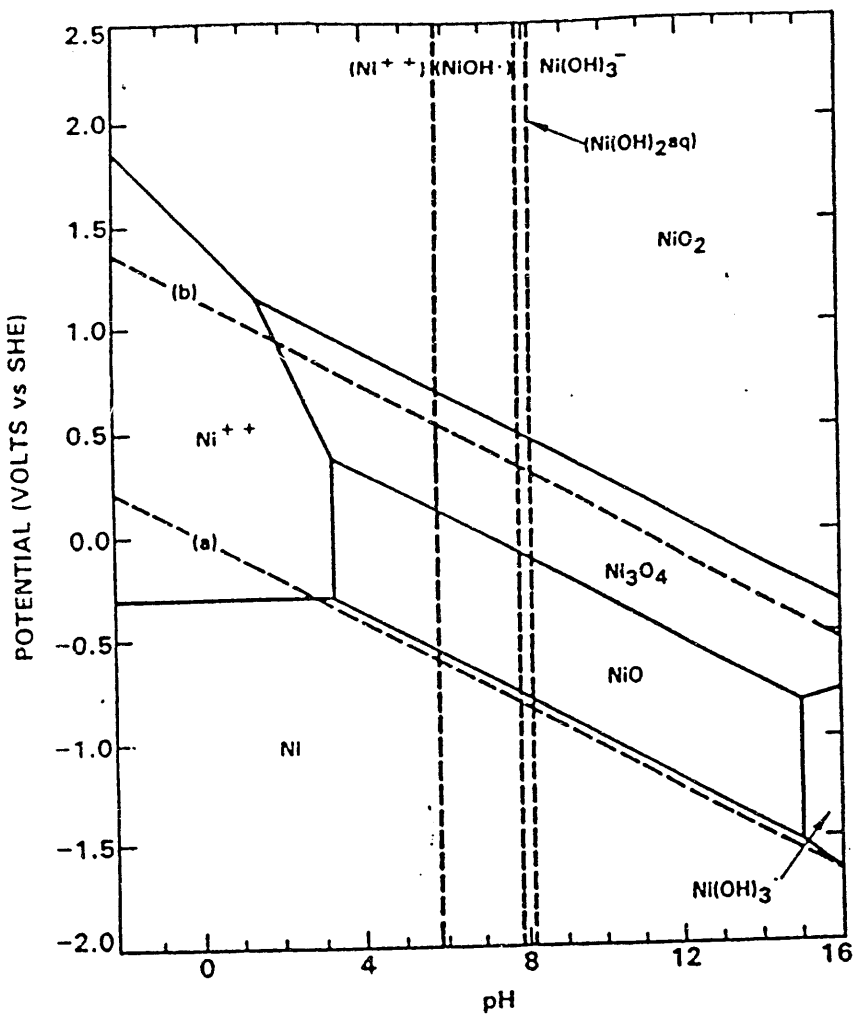

Figure 11 Potential pH diagram for the Ni-water system (at 288°C) with dissolved species activities of 10^{-3}.(ref)

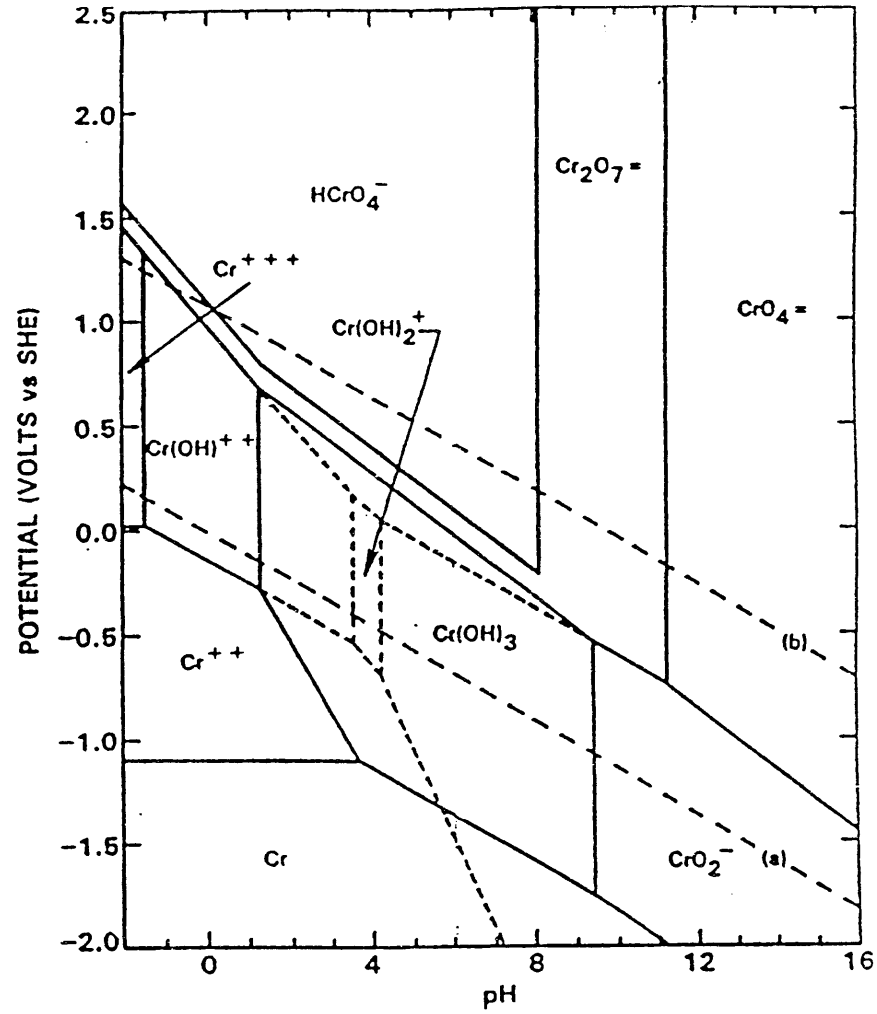

Figure 12 Potential pH diagram for the Cr-water system (at 288°C) with dissolved species activities of 10^{-3}.(ref)

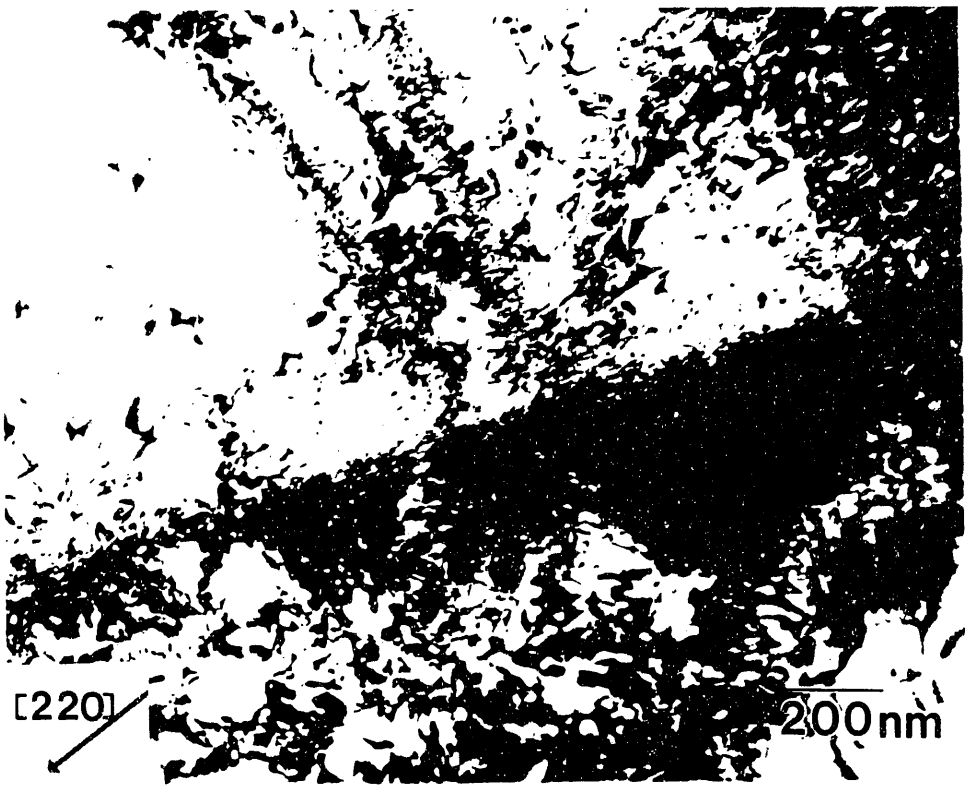

Figure 13 Dislocation structure in the UHP alloy after 8% deformation.

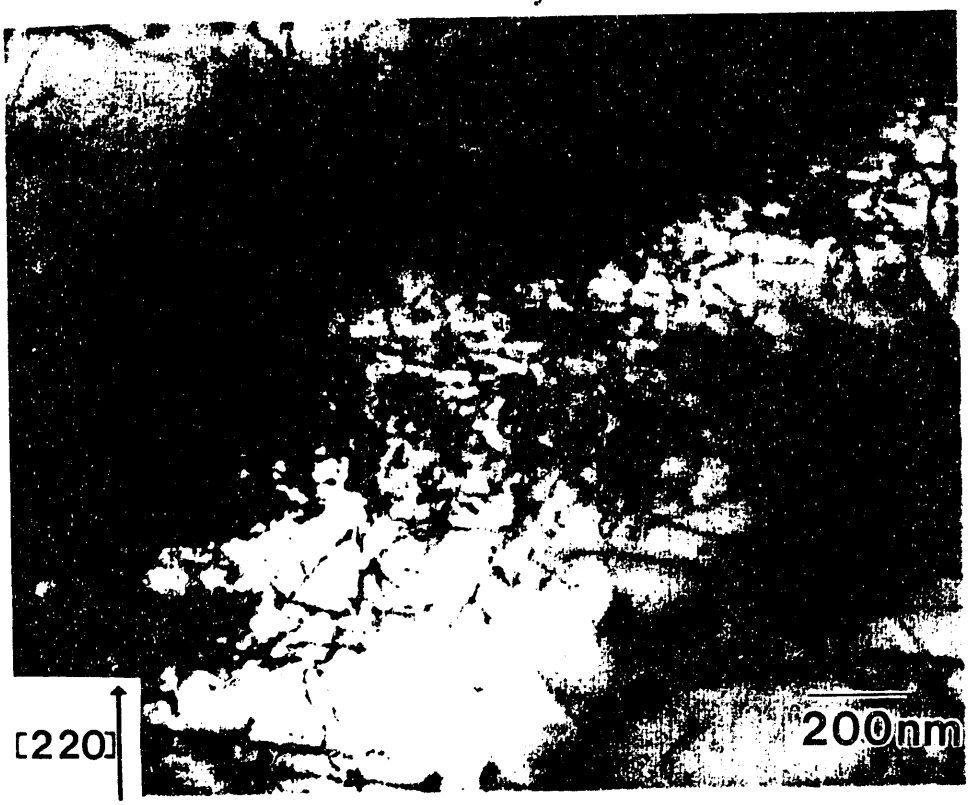

Figure 14 Dislocation structure in the CD alloy after 8% deformation.

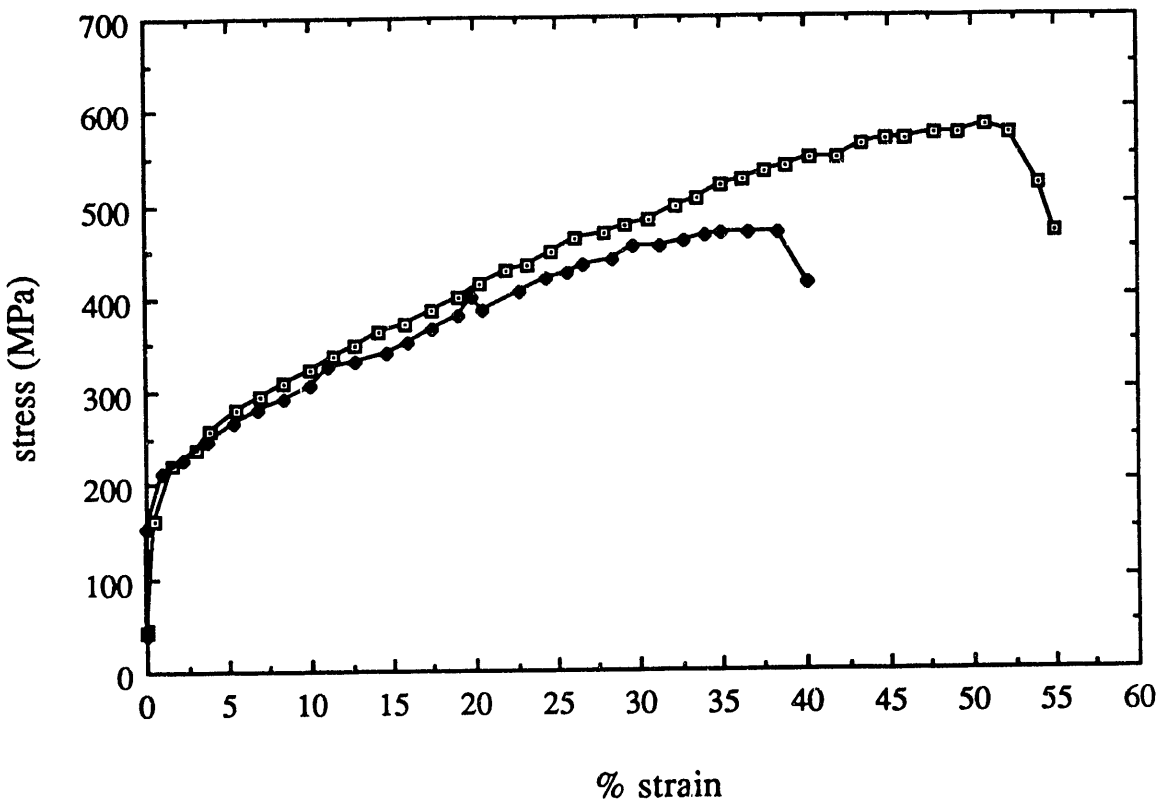

Figure 15 Constant extension rate tensile experiment of alloys CD and UHP in 345°C argon at $1 \times 10^{-6}\ s^{-1}$.

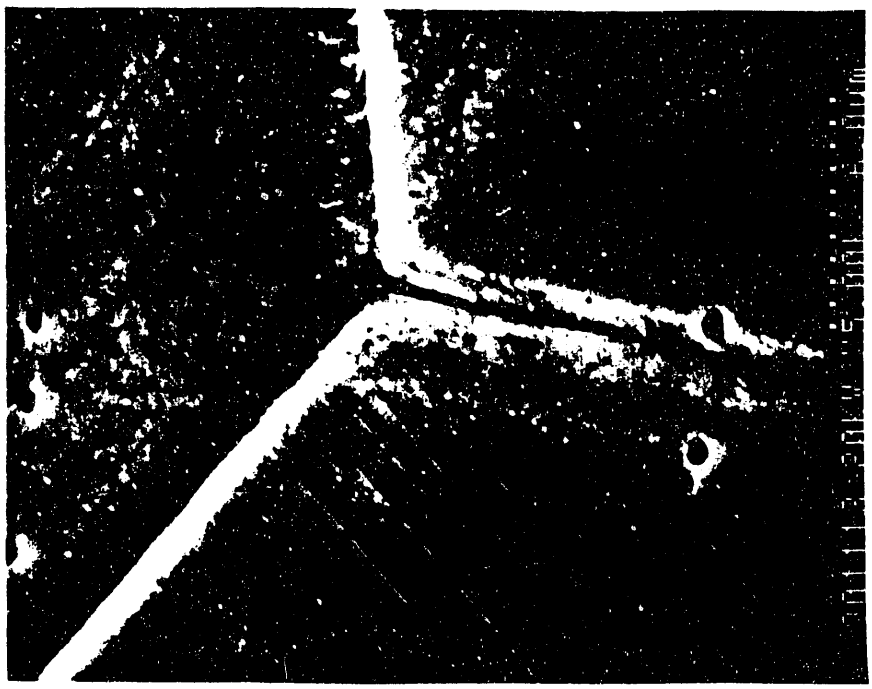

Figure 16 A typical wedge shape crack at a high angle boundary following a creep experiment at 300 MPa in 360°C Argon.

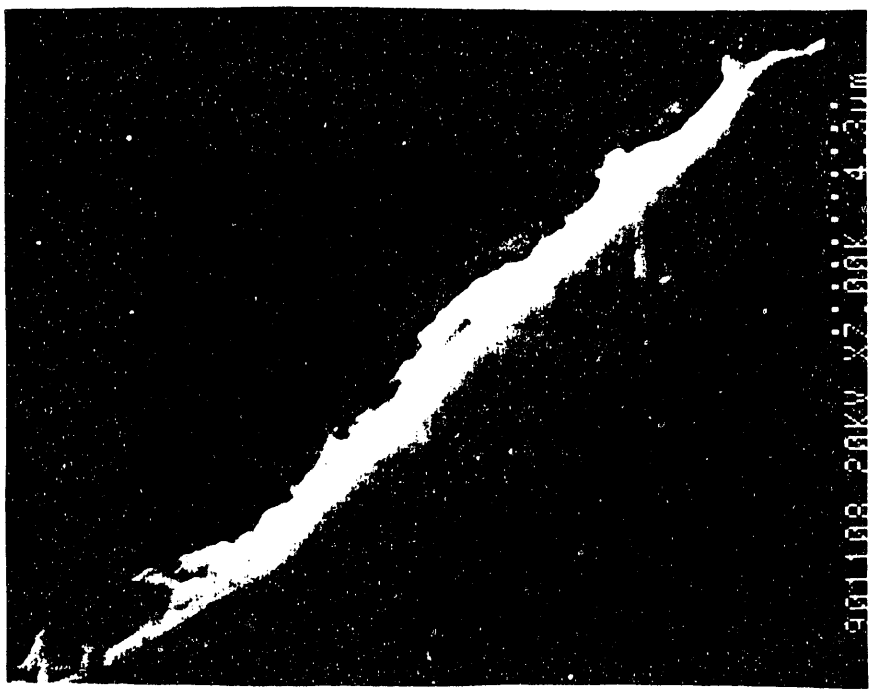

Figure 17 Cavities in the matrix near the high angle boundary of the sample shown in Fig. 16.

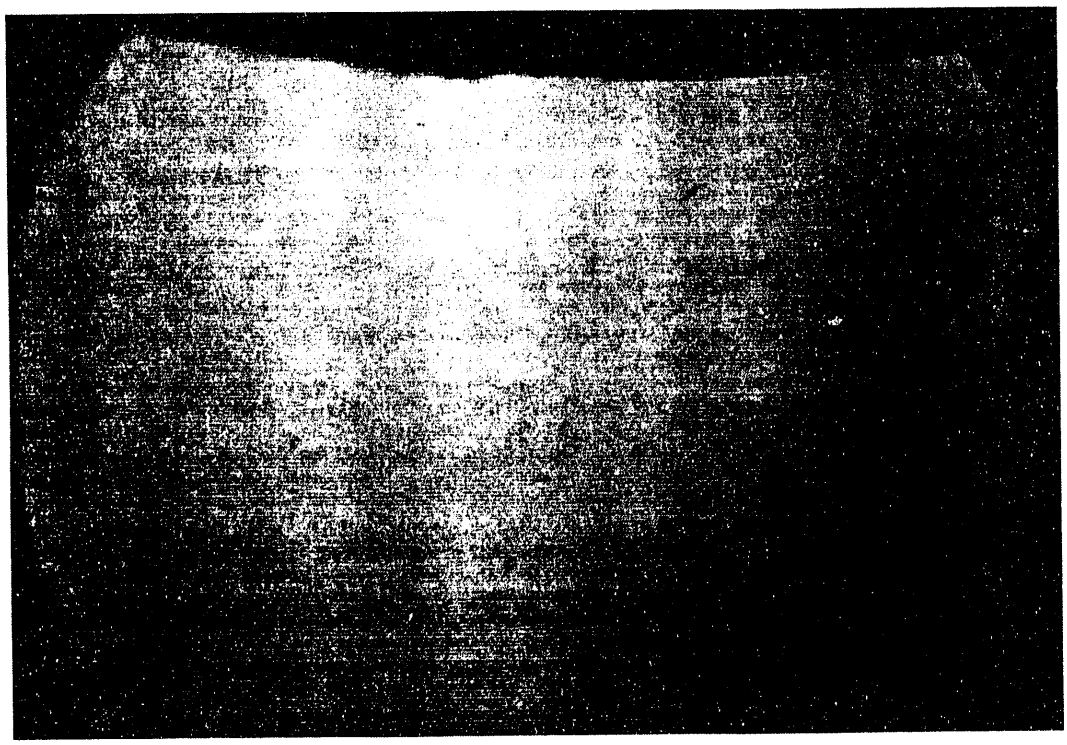

Figure 18 An example of Electron Back-Scattering Pattern (EBSP) captured on the Macintosh II with the current set up.

END

DATE FILMED

12 / 14 / 92